LETTERS

Label-free immunodetection with CMOS-compatible semiconducting nanowires

Eric Stern[1], James F. Klemic[2], David A. Routenberg[2], Pauline N. Wyrembak[5], Daniel B. Turner-Evans[2], Andrew D. Hamilton[5], David A. LaVan[3], Tarek M. Fahmy[1] & Mark A. Reed[2,4]

Semiconducting nanowires have the potential to function as highly sensitive and selective sensors for the label-free detection of low concentrations of pathogenic microorganisms[1–10]. Successful solution-phase nanowire sensing has been demonstrated for ions[3], small molecules[4], proteins[5,6], DNA[7] and viruses[8]; however, 'bottom-up' nanowires (or similarly configured carbon nanotubes[11]) used for these demonstrations require hybrid fabrication schemes[12,13], which result in severe integration issues that have hindered widespread application. Alternative 'top-down' fabrication methods of nanowire-like devices[9,10,14–17] produce disappointing performance because of process-induced material and device degradation. Here we report an approach that uses complementary metal oxide semiconductor (CMOS) field effect transistor compatible technology and hence demonstrate the specific label-free detection of below 100 femtomolar concentrations of antibodies as well as real-time monitoring of the cellular immune response. This approach eliminates the need for hybrid methods and enables system-scale integration of these sensors with signal processing and information systems. Additionally, the ability to monitor antibody binding and sense the cellular immune response in real time with readily available technology should facilitate widespread diagnostic applications.

We demonstrate here that the limitations of fabricated nanowire-type devices can be overcome and that nanometre-scale sensors with little mobility degradation from bulk can be achieved. We have used ultrathin silicon-on-insulator wafers[9,10,18,19], which require only lateral (in-plane, two-dimensional) active layer definition to achieve the nanometre dimensions needed for a nanowire-type device. Previous attempts with this approach used reactive-ion etching (RIE) of the active silicon layer, which unacceptably degraded device performance[9,10]. To achieve the nanometre-scale dimensions necessary for sensitivity, we developed a fabrication process using an anisotropic wet etch: specifically, tetramethylammonium hydroxide, TMAH, which etches Si (111) planes about 100 times more slowly than all other planes[20]. This approach allows retention of pattern definition (of a masking oxide layer), and smoothes edge imperfections not aligned to the (111) plane. Previous work on TMAH-defined electronic devices has shown excellent retention of electrical properties[18], although not in configurations suitable for sensing. We show that 'nanowire' devices capable of sensing can be defined by TMAH etching. Our approach uses commercially available (100) silicon-on-insulator wafers that yield trapezoidal cross-section nanowires with dominant Si (111) exposed planes, the preferred surface for selective surface functionalization[21].

First, we show that this process can be used reproducibly to generate non-degraded devices that are narrower than their lithographic pattern definition[19]. A schematic depicting a completed device before removal of the masking oxide is shown in Fig. 1a. The anisotropic wet etch undercuts this masking oxide, whose lateral dimensions can be achieved with optical lithography, although it does not appreciably etch the degenerately doped ($>10^{20}$ cm^{-3}) boron contacts[20]. A top-view scanning electron micrograph of a device with the oxide mask

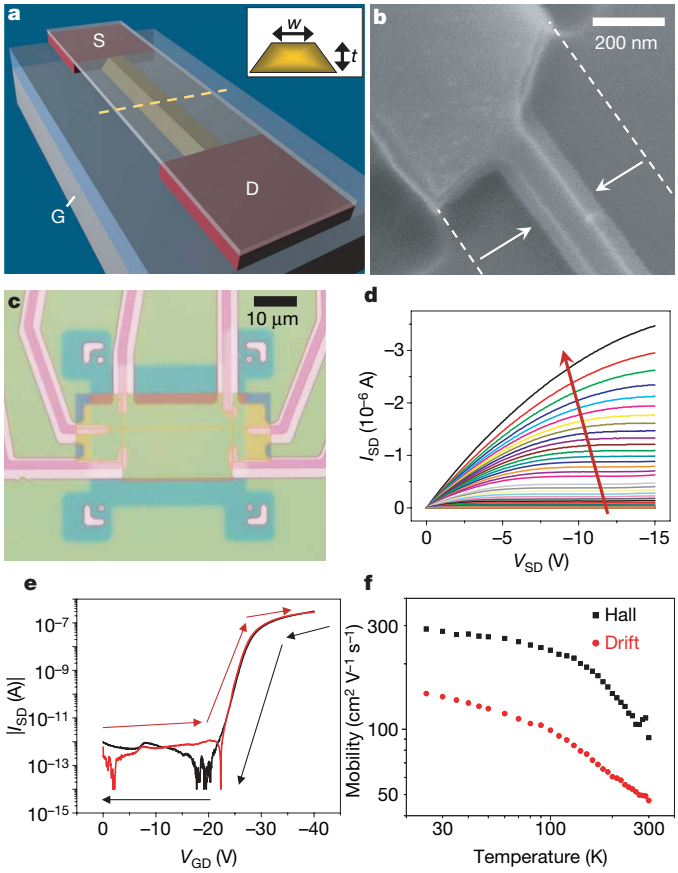

Figure 1 | Device fabrication and electrical performance. **a**, Schematic after anisotropic etch. The silicon-on-insulator active channel (yellow, width w and thickness t) is undercut etched, whereas degenerate leads (red) are etch-resistant. The source (S), drain (D), and underlying backgate (G) are labelled. **b**, **c**, Scanning electron micrograph (**b**) and optical micrograph (**c**) of a completed device. **d**, $I_{SD}(V_{SD})$ ($w = 50$nm, $t = 25$nm) for varying V_{GD} (0 to -40 V, $\Delta V = -1$ V), illustrating p-type accumulation mode behaviour. **e**, $|I_{SD}|(V_{GD})$ for $V_{SD} = -1$ V for forward (red) and reverse (black) sweep. **f**, Accumulation-mode Hall and drift mobilities versus temperature ($w = 300$ nm, $t = 25$ nm).

[1]Department of Biomedical Engineering, [2]Department of Electrical Engineering, [3]Department of Mechanical Engineering, [4]Department of Applied Physics, Yale University, P O Box 208284 New Haven, Connecticut 06511, USA. [5]Department of Chemistry, Yale University, P O Box 208107, New Haven, Connecticut 06511, USA.

removed (Fig. 1b) illustrates its trapezoidal shape. Although pattern-definition roughness is evident at the contact regions, the nanowire has no such roughness, owing to the planarization of the etch. Reproducible and well-controlled device narrowing (Supplementary Fig. 3) is achieved owing to the slow Si (111) etch rate. The fabrication approach is flexible, allowing for the configuration of a variety of nanowire geometries, such as a six-point, Hall bar device (see optical micrograph in Fig. 1c). The CMOS compatibility of the technique enables the simultaneous fabrication of sensor arrays, complementary error detection[9,10], and integrated signal processing electronics. Although nanowire arrays fabricated with this process may not be capable of achieving the ultrahigh densities attainable with other approaches, considerations including Debye screening length (λ_D)[9], length of functionalization molecules, and macromolecular size may render ultrahigh density arrays suboptimal for sensing applications.

Electrical characterization verifies that this fabrication approach produces high-quality devices. The source–drain current (I_{SD}) versus source–drain voltage (V_{SD}) dependence for varying gate–drain voltage (V_{GD}) is shown in Fig. 1d, and the $I_{SD}(V_{GD})$ dependence for constant V_{SD} in Fig. 1e, for a representative p-type device. The small hysteresis between forward and reverse $I_{SD}(V_{GD})$ slopes suggests minimal defect-induced charge trapping. Peak drift mobilities were calculated from the measured $I_{SD}(V_{GD})$ dependence and a self-consistent device simulation (Silvaco program; www.silvaco.com); averaged across 12 devices, we obtain 54 $cm^2 V^{-1} s^{-1}$, with a maximum of 139 $cm^2 V^{-1} s^{-1}$. These results compare favourably with p-type silicon doped to 10^{15} cm^{-3}, which has a bulk mobility of 450 $cm^2 V^{-1} s^{-1}$ at 300 K (ref. 22), and the known decrease in mobility for high field and anisotropically defined Si (111) planes[23]. The ability to produce nanowires in a Hall bar geometry allows measurement of the Hall mobility in a nanowire for the first time to our knowledge, Fig. 1f. Ongoing studies are examining drift versus Hall mobilities and their utility in determining scattering mechanisms.

To characterize liquid-phase sensor response, a macro-scale solution chamber was designed specifically to avoid the well-characterized limits on sensitivity and response time inherent in diffusion-limited systems such as microchannels[24]. Our design (Fig. 2a) is experimentally simple and induces mixing during fluid exchange, and was used for all solution-based sensor measurements.

Unfunctionalized devices were characterized as hydrogen ion sensors; the oxide that coats the exposed silicon nanowire surfaces (top and sides) can be protonated and deprotonated by varying pH, which in turn gates the underlying device, thereby modulating I_{SD} (refs 3, 25). The response of a large and small device to five solutions with pH values varying from 6.0–8.0 is displayed in Fig. 2b. Consistent with p-type semiconducting behaviour, the source–drain conduction decreases as the acidity of the solution increases. Both devices respond appropriately to pH changes (linearly on a logarithmic current scale), with the smaller device exhibiting greater sensitivity: the pH 8.0/pH 6.0 current ratio is 43.8 versus 11.4 (for the smaller versus the larger device, respectively). The impact of scaling on sensitivity is illustrated in Fig. 2c and the TMAH-etched devices were found to scale with inverse surface area. The sensor response of a 3-μm-wide RIE edge-defined control structure processed simultaneously with the TMAH-etched devices is also shown in Fig. 2c. This device is nominally identical with the exception of channel definition, and illustrates RIE-induced degradation of sensing performance.

To demonstrate the efficacy of these sensors in monitoring real-time cellular responses, we analysed the well-characterized system of T-lymphocyte activation[26]. Antibody-mediated crosslinking of cell-surface CD3 ligands triggers activation of T cells, inducing intracellular signalling and subsequent effector mechanisms. One consequence of such activation includes the release of acid[27]. Addition of species-specific antibody directed against the mouse CD3 complex

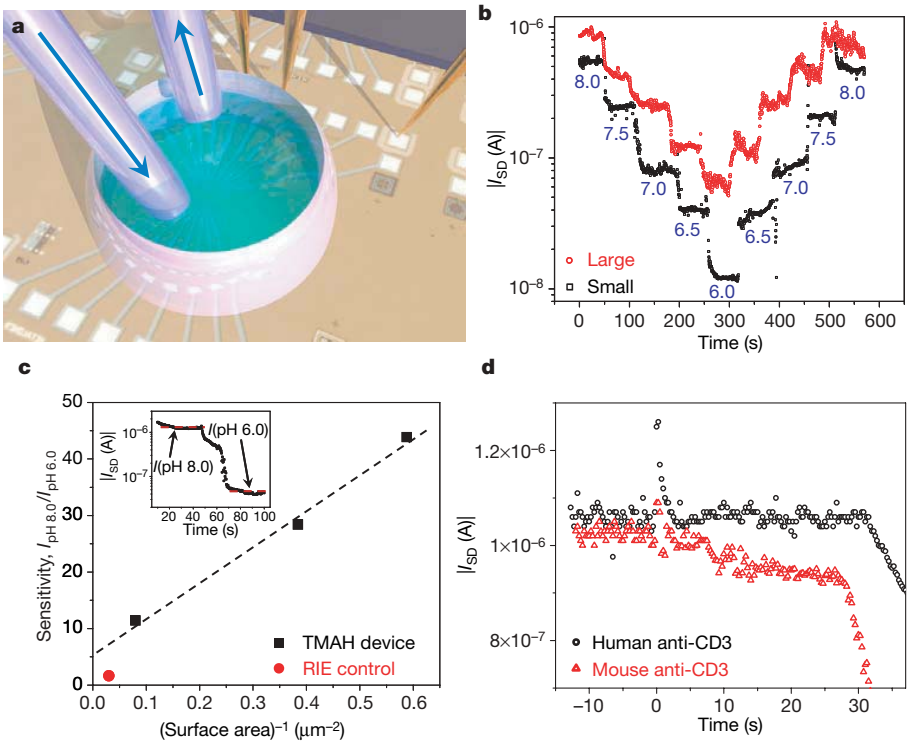

Figure 2 | Unfunctionalized device sensing. **a**, Schematic of fluid exchange system superimposed on chip optical micrograph. Fluid supply and return (arrows) are provided by Tygon tubes. **b**, Response of two sensors to five solutions of different pH (indicated in blue). Large sensor: $w = 1{,}000$ nm, $t = 80$ nm. Small sensor: $w = 100$ nm, $t = 25$ nm. **c**, Device sensitivity versus inverse device surface area. The inset shows the sensitivity definition. **d**, Response of devices with $w = 100$ nm and $t = 40$ nm to changes in extracellular pH. A non-immune (human anti-CD3, black) and immune (mouse anti-CD3, red) stimulant were added to ~6,000 mouse-derived T cells at time zero.

(mouse-anti-CD3) to a suspension of mouse splenocytes containing T cells caused a current decrease after ~10 s and a continued negative derivative, Fig. 2d. In contrast, a control experiment with a species-specific antibody to human CD3 showed no response. Device instability was observed at ~30 s, although preliminary measurements have indicated that unintentional solution-to-backgate leakage in the present device design may be the cause. These data are consistent with previous results obtained with a microphysiometer[27] and with expectations regarding early signals responsible for T-cell activation that involve clustering of CD3 receptors[26].

Another powerful application of these devices is the direct detection of macromolecules without the need for the a priori attachment of fluorescent, radioactive or other probes to those macromolecules, that is, label-free sensing. Specific detection using this approach therefore requires that the nanowire be functionalized with a receptor for the unlabelled macromolecule. To maximize device sensitivity, only the nanowire should be functionalized, because nonspecific functionalization of both the nanowire and the underlying oxide will greatly diminish sensitivity owing to binding competition[3,4,6–8,10]. We used dec-9-enyl-carbamic acid tert-butyl ester for functionalization because this molecule has previously been shown to confer amine functionality selectively to silicon[28], and we found that device performance is preserved after functionalization with this olefin (Supplementary Fig. 5b). Electrically directed functionalization[21] was achieved (Supplementary Fig. 6) but was found to unacceptably degrade device performance (Supplementary Fig. 5e), most probably by creating redox-active surface traps.

Sensitivity to protein binding was characterized using the well-known biotin-avidin/streptavidin interaction. To avoid the problem of Debye screening[9], the salt concentrations in the buffers used for macromolecular sensing experiments were chosen such that λ_D was sufficiently long to enable sensing, but sufficiently short to screen unbound macromolecules[29]. We first determined biotinylated[30] device responses to streptavidin, biotin-quenched streptavidin (streptavidin pre-treated with five equivalents of biotin), and avidin (all 1 nM); see Fig. 3a. The addition of streptavidin resulted in a current increase due to the protein's negative charge, whereas the previously quenched streptavidin elicited no response (separately, fluorescently conjugated streptavidin was bound and fluorescently imaged; see inset to Fig. 3a). In contrast, upon introduction of avidin, the current decreased due to the protein's positive charge. A poly(ethylene glycol) (PEG)-functionalized control device yielded no response to 1 nM streptavidin addition with the exception of injection transient noise, which is observed in all measurements. Complementary devices, necessary for error detection, demonstrated opposite polarity (Supplementary Fig. 7).

To demonstrate unequivocally that the biotin–streptavidin interaction was responsible for sensor response, biotinylation of one device was performed with a cleavable molecule (SS-biotin), while a second device was biotinylated with a non-cleavable molecule (LC-biotin)[30]. The initial response of each sensor to 1 nM streptavidin is similar (Fig. 3b). The subsequent addition of a reducing agent cleaved the disulphide bond[21], with the resultant current for the SS-biotinylated device returning to the original baseline value, whereas the LC-biotinylated control was insensitive to the reducing agent.

Device sensitivity to protein charge and concentration, the hallmarks of nanowire-field effect transistor sensing, were also studied. Avidin is positive in neutral solutions owing to its high isoelectric point (pI ≈ 10.5), but its effective charge can be decreased by increasing solution pH. Figure 3c demonstrates decreased device sensitivity with increasing solution pH (1 nM avidin). Thus, to optimize protein sensing, it is imperative that the $|pH_{solution} - pI|$ be maximized. (Alternatively, with the use of a linear solution pH gradient, this platform could be used to determine unknown protein pI values.)

An exploration of the detection limit of these sensors is shown in Fig. 3d, where streptavidin concentrations are decreased from 1 nM to 10 fM. Close inspection of the post-transition current reveals that the response at the highest protein concentrations saturates (probably fully coating the sensor with bound protein during solution exchange), whereas the signal continues to increase for proteins in the solutions of lower concentration, probably owing to continued diffusion and binding to the devices after initial mixing. The 10 fM solution has an initial signal-to-noise response of 140, implying a detection floor of ~70 aM.

Device utility for immunodetection applications using antibodies was demonstrated with commercially available antibodies to mouse immunoglobulin G (IgG) and mouse immunoglobulin A (IgA) proteins. A cross-comparison assay was performed by first functionalizing two devices with goat anti-mouse IgG and two additional devices with goat anti-mouse IgA[30]. Devices from each group were then used to sense 100 fM antigen. Figure 4 shows clear discrimination (after injection transient noise) of the specific antigen over the nonspecific

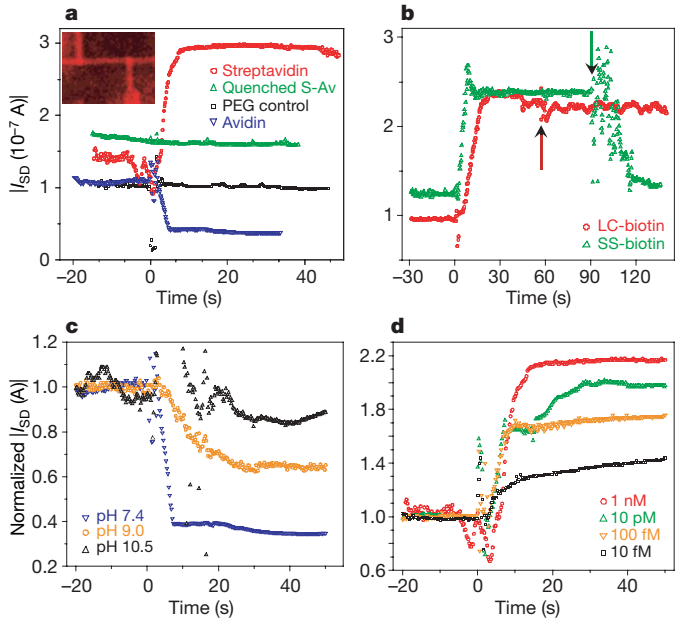

Figure 3 | Protein detection and sensitivity. Solution exchange occurs at time zero. **a**, Specific recognition and protein charge determination of avidin/streptavidin. All additions used 1 nM solutions. Inset shows fluorescence micrograph of biotin-functionalized device after fluorescently labelled streptavidin addition. **b**, Verification of surface charge by cleavage. Streptavidin (1 nM) addition to LC-biotin- or SS-biotin-functionalized devices. The arrow indicates reducing agent (TCEP) addition. **c**, Biotinylated sensor response to protein charge, by addition of 1 nM avidin in buffers with different pH values. **d**, Detection response with decreasing streptavidin concentration. For **c** and **d**, currents were normalized by dividing the measured I_{SD} by the pre-addition average current.

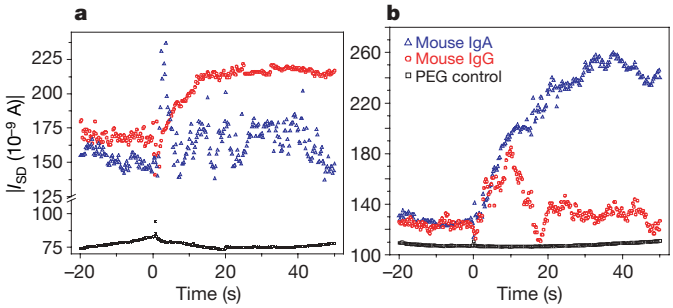

Figure 4 | Demonstration of immunodetection. All solution exchanges occurred at time zero. Sensor responses to 100 fM mouse-IgG (red) or 100 fM mouse-IgA (blue) for goat anti-mouse IgG-functionalized sensor (**a**) or goat anti-mouse IgA-functionalized sensor (**b**). The PEG-functionalized sensor control is shown in black.

control for the reciprocal cases, demonstrating selective immunodetection. Thus, the ability of this approach to specifically detect antibodies at less than 100 fM concentrations (also with complementary electronic response; see Supplementary Fig. 7c) has been shown.

We have thus demonstrated a novel approach for realizing integrable silicon nanowire sensors for less than 100 fM specific label-free antibody detection, as well as for monitoring real-time live cellular response. Although this study focused on device and sensor performance, the strength of the approach lies in seamless integration with CMOS technology. While device integration and reliability issues (including high-reliability selective functionalization) should not be trivialized, our approach appears to have potential for extension to a fully integrated system, with wide use as sensors in molecular and cellular arrays.

METHODS

For detailed descriptions of device fabrication, organic synthesis and device functionalization, see the Supplementary Information.

General sensing parameters. In all experiments I_{SD} was measured at 0.25 s intervals. Unfunctionalized sensor measurements used $V_{SD} = -5$ V and $V_{GD} = -33$ V, while for functionalized-sensor measurements, $V_{SD} = -2$ V and $V_{GD} = -20$ V. Mixing was continued after injection of the solution of interest.

Macromolecule sensing. All devices used for functionalized-sensing experiments were nominally similar, with channel thickness $t = 40$ nm and width $w = 50$–150 nm. Each measurement was produced by a distinct device.

Received 2 August; accepted 30 November 2006.

1. Lim, D. V., Simpson, J. M., Kearns, E. A. & Kramer, M. F. Current and developing technologies for monitoring agents of bioterrorism and biowarfare. *Clin. Microbiol. Rev.* **18,** 583–607 (2005).
2. Madou, M. J. & Cubicciotti, R. Scaling issues in chemical and biological sensors. *Proc. IEEE* **91,** 830–838 (2003).
3. Cui, Y., Wei, Q., Park, H. & Lieber, C. M. Nanowire nanosensors for highly sensitivie and selective detection of biological and chemical species. *Science* **293,** 1289–1292 (2001).
4. Wang, W. U., Chen, C., Lin, K.-h., Fang, Y. & Lieber, C. M. Label-free detection of small-molecule-protein interactions by using nanowire nanosensors. *Proc. Natl Acad. Sci. USA* **102,** 3208–3212 (2005).
5. Tang, T. *et al.* Complementary response of In_2O_3 nanowires and carbon nanotubes to low-density lipoprotein chemical gating. *Appl. Phys. Lett.* **86,** 103903 (2005).
6. Zheng, G., Patolsky, F., Cui, Y., Wang, W. U. & Lieber, C. M. Multiplexed electrical detection of cancer markers with nanowire sensor arrays. *Nature Biotechnol.* **23,** 1294–1301 (2005).
7. Hahm, J.-i. & Lieber, C. M. Direct ultrasensitivie electrical detection of DNA and DNA sequence variations using nanowire nanosensors. *Nano Lett.* **4,** 51–54 (2004).
8. Patolsky, F. *et al.* Electrical detection of single viruses. *Proc. Natl Acad. Sci. USA* **101,** 14017–14022 (2004).
9. Cheng, M. M.-C. *et al.* Nanotechnologies for biomolecular detection and medical diagnostics. *Curr. Opin. Chem. Biol.* **10,** 11–19 (2006).
10. Li, Z. *et al.* Sequence-specific label-free DNA sensors based on silicon nanowires. *Nano Lett.* **4,** 245–247 (2004).
11. Chen, R. J. *et al.* An investigation of the mechanisms of electronic sensing of protein adsorption on carbon nanotube devices. *J. Am. Chem. Soc.* **126,** 1563–1568 (2004).
12. Huang, Y., Duan, X., Wei, Q. & Lieber, C. M. Directed assembly of one-dimensional nanostructures into functional networks. *Science* **291,** 630–633 (2001).
13. Evoy, S. *et al.* Dielectrophoretic assembly and integration of nanowire devices with functional CMOS operating circuitry. *Microelect. Eng.* **75,** 31–42 (2004).
14. Englander, O., Christensen, D., Kim, J., Lin, L. & Morris, S. J. S. Electric-field assisted growth and self-assembly of intrinsic silicon nanowires. *Nano Lett.* **5,** 705–708 (2005).
15. Elibol, O. H., Morisette, D., Akin, D., Denton, J. P. & Bashir, R. Integrated nanoscale silicon sensors using top-down fabrication. *Appl. Phys. Lett.* **83,** 4613–4615 (2003).
16. Clement, N. *et al.* Electronic transport properties of single-crystal silicon nanowires fabricated using an atomic force microscope. *Physica E* **13,** 999–1002 (2002).
17. Wang, D., Sheriff, B. A. & Heath, J. R. Silicon p-FETs from ultrahigh density nanowire arrays. *Nano Lett.* **6,** 1096–1100 (2006).
18. Liu, Y., Ishii, K., Tsutsumi, T., Masahara, M. & Suzuki, E. Ideal rectangular cross-section Si-fin channel double-gate MOSFETs fabricated using orientation-dependent wet etching. *IEEE Elect. Dev. Lett.* **24,** 484–486 (2003).
19. Saitoh, M., Murakami, T. & Hiramoto, T. Large Coulomb blockade oscillations at room temperature in ultranarrow wire channel MOSFETs formed by slight oxidation process. *IEEE Trans. Nanotech.* **2,** 241–245 (2003).
20. Tabata, O., Asahi, R., Funabashi, H., Shimaoka, K. & Sugiyama, S. Anisotropic etching of silicon in TMAH solutions. *Sensors Actuators A* **34,** 51–57 (1992).
21. Bunimovich, Y. L. *et al.* Electrochemically programmed, spatially selective biofunctionalization of silicon wires. *Langmuir* **20,** 10630–10638 (2004).
22. Sze, S. M. *Physics of Semiconductor Devices* 2nd edn 849 (John Wiley & Sons, New York, 1981).
23. Sun, S. C. & Plummer, J. D. Electron mobility in inversion and accumulation layers on thermally oxidized silicon surfaces. *IEEE J. Solid-State Circuits* **15,** 562–573 (1980).
24. Sheehan, P. E. & Whitman, L. J. Detection limits for nanoscale biosensors. *Nano Lett.* **5,** 803–807 (2005).
25. Laws, G. M. *et al.* Molecular control of the drain current in a buried channel MOSFET. *Phys. Status Solidi B* **233,** 83–89 (2002).
26. Trautmann, A. Microclusters initiate and sustain T cell signaling. *Nature Immunol.* **6,** 1213–1214 (2005).
27. Beeson, C. *et al.* Early biochemical signals arise from low affinity TCR-ligand reaction at the cell-cell interface. *J. Exp. Med.* **184,** 777–782 (1996).
28. Strother, T., Hamers, R. J. & Smith, L. M. Covalent attachment of oligodeoxyribonucleotides to amine-modified Si (001) surfaces. *Nucleic Acids Res.* **28,** 3535–3541 (2000).
29. Israelachvili, J. N. *Intermolecular and Surface Forces with Applications to Colloidal and Biological Systems* Ch. 12 (Academic Press, New York, 1985).
30. Hermanson, G. T. *Bioconjugate Techniques* Ch. 1–3, 5, 7 8 (Elsevier Science & Technology Books, New York, 1996).

Supplementary Information is linked to the online version of the paper at www.nature.com/nature.

Acknowledgements We thank R. Ilic, D. Westly, M. Metzler and V. Genova (Cornell Nanofabrication Facility) for device processing assistance; T. Ma, R. Sleight, J. Hyland, M. Young and C. Tillinghast for device processing discussions; F. Sigworth and D. Stern for functionalization and sensing discussions and for assistance in manuscript preparation; M. Saltzman, K. Klemic, A. Flyer, J. Bertram and S. Jay for functionalization and sensing discussions; Z. Jiang for scanning electron micrograph imaging assistance; S. R. Lee for Silvaco simulations; and R. Munden for device measurement assistance. This work was partially supported by DARPA through ONR and AFOSR (M.A.R.), NASA (M.A.R.), the NIH (A.D.H.), the Coulter Foundation (T.M.F.), by a Department of Homeland Security graduate fellowship (E.S.), and by a N.S.F. graduate fellowship (E.S., D.A.R.). This work was performed in part at the Cornell Nanoscale Science and Technology Facility, a member of the National Nanotechnology Infrastructure Network that is supported by the NSF.

Author Contributions E.S. performed device fabrication and measurements. J.F.K. assisted in fabrication design, D.A.R. performed device mobility experiments and analysis, and P.N.W. and A.D.H. provided molecules used for device functionalization. D.T-E. assisted in device characterization. E.S. and T.M.F. performed T-cell isolation and T-cell measurements. D.A.L., T.M.F. and M.A.R. contributed to experimental design, characterization and interpretation. E.S., J.F.K., T.M.F. and M.A.R. analysed the data and wrote the manuscript with contributions from all authors.

Author Information Reprints and permissions information is available at www.nature.com/reprints. The authors declare no competing financial interests. Correspondence and requests for materials should be addressed to M.A.R. (mark.reed@yale.edu) or T.M.F. (tarek.fahmy@yale.edu).